Supplementary Material

Fazle Hussain, Edgardo García, Jie Yao, Eric Stout

S1 Flow separation criteria

For separated flows, one key issue is to determine the detachment and reattachment locations. Previously, we used the mean dividing streamline to determine these locations, but other approaches have been proposed. Hence, it is worthwhile to compare these criteria, particularly in the presence of roughness. The separation location is often defined as the point at which the mean streamwise velocity component approaching the wall (along the limiting streamline) becomes zero, therefore $\langle \tau_w \rangle = 0$. Necessarily, if the streamwise velocity component near the wall goes to zero, due to continuity, the velocity vector will form a 90° angle with the wall. Thus, as suggested by Wu & Piomelli (2018), one indicator of flow separation is the angle of the velocity vector with respect to the wall $\Theta = cos^{-1}[(U_i s_i)/(\sqrt{U_k U_k}\sqrt{s_j s_j})]$, where s_i are the components of the vector parallel to the wall. Another criterion is based on the intermittency of flow reversal – defined as the fraction of time the flow goes downstream, $\gamma_u = \sum t[U < 0]/\sum t$ – is 50% and called transitory detachment, i.e. $\gamma_u = 0.5$ (Simpson, 1989; Simpson *et al.*, 1981). For the SW case, detachment and reattachment locations in the spanwise direction is the same and readily characterized by the mean streamlines (see main paper) and reported in table 1 for all methods mentioned. All criteria yield roughly the same result, which is consistent with the previous finding by Na & Moin (1998).

Wu & Piomelli (2018) showed that locations with $\gamma_u = 0.5$ fail when random wall roughness is present. The color maps of $\langle \tau_w \rangle$ for the GW case (see paper), provide insight into the spanwise heterogeneity of the locations of detachment and reattachment. Locations of $\langle \tau_w \rangle = 0$ (denoted by the dashed black line) agree with the locations of detachment and reattachment characterized by the mean dividing streamline (see the mean streamlines in the paper) for the crests and troughs. The intermittency of forwarding flow, γ_u, at the wall is shown in figure 1. The separation location determined by $\gamma_u = 0.5$ also agrees with the location of $\langle \tau_w \rangle = 0$. The only notable difference is the secondary recirculation bubble inside the groove (see in the main paper mean streamlines at $x = 4.8$) where $\gamma_u = 0.5$ shows a bigger secondary recirculating streamwise length with respect to that obtained with $\langle \tau_w \rangle = 0$. Finally, figure 2 shows the flow angle with respect to the wall. This criterion sharply indicates regions of backward flow near the wall and perfectly agrees with $\langle \tau_w \rangle = 0$. Although the grooves behave as a fully rough element at the peak of the bump, we find that the definitions of flow detachment/reattachment based on all these criteria agree with each other, in contrast to the observations for random roughness. This is perhaps because the grooves are purely longitudinal so that they do not add any extra form drag to the flow over the bump. It would be interesting to see whether such an agreement holds true for the transversal grooves, which induce local recirculation regions within the larger separated region caused by the bump.

It is rather challenging to experimentally measure skin friction at the wall. Additionally, there is large uncertainty when considering complex roughness elements either numerically (Bailon-Cuba *et al.*, 2009; Gatti & Quadrio, 2016) or experimentally (Song & Eaton, 2002). For these reasons, flow separation criteria are typically computed at the crests of the roughness elements after spatial averages; like in the present work, one could also consider the overall effect of roughness on the overlying flow by averaging along the spanwise direction. As a point of reference, we report in table 1 the reattachment position (x_r) for various flow separation criteria from the spanwise averaged field, and all are in agreement. Again, this agreement can be attributed to the organized nature of the roughness. While these estimates remain reasonable on the back of the bump for the detachment and reattachment points at crests, they underestimate the reattachment location within the troughs. The primary shortcoming of estimating the separation location from the z-averaged field is that it completely overlooks the flow separation in the upstream side of the bump inside the grooves and the minibubble inside the grooves on the downstream side of the bump. Therefore, any recirculation region that does not extend well above the roughness elements will be missed, likewise, when detachment/reattachment

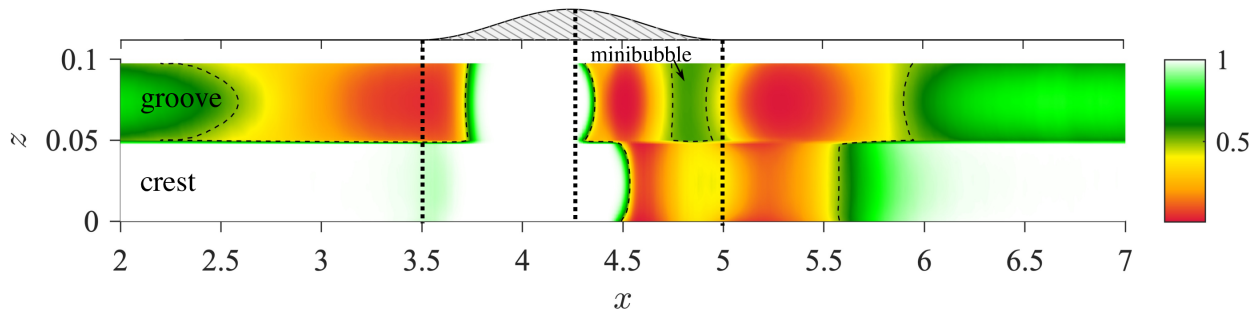

Figure 1: Color maps of intermittency of forward flow (γ_u) at the wall. The dashed line contour corresponds to $\gamma_u = 0.5$; the top half is the groove.

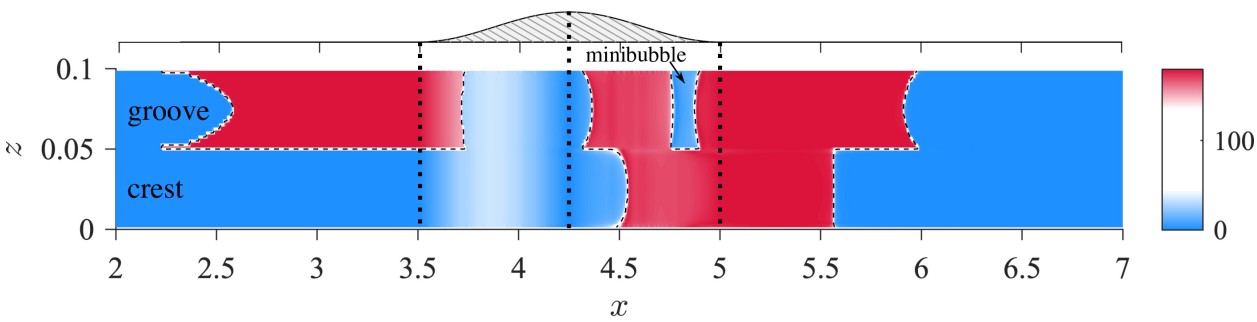

Figure 2: Color maps of the flow angle with respect to the wall surface (Θ) in degrees. The dashed line contour corresponds to 90°; top half is the groove.

locations occur within cavities of the roughness. Thus, accurately capturing separated regions below the heights of the roughness elements remains a challenge, though larger separated regions are well captured for our organized roughness using existing methods.

S2 TKE production and Reynolds stress components

The Reynolds stress balances are reported at the position of negative production and peak of production. The transport equation for the Reynolds stresses is

$$\frac{\partial \langle U_k \rangle \langle u_i' u_j' \rangle}{\partial x_k} = \mathcal{P}_{ij} + \epsilon_{ij} + T_{ij} + \Pi_{ij} + V_{ij}, \tag{1}$$

where $\mathcal{P}_{ij} = -\langle u_i' u_k' \rangle \partial \langle U_j \rangle / \partial x_k - \langle u_j' u_k' \rangle \partial \langle U_i \rangle / \partial x_k$ is the production tensor, $\epsilon_{ij} = 2/Re \langle \partial u_i' / \partial x_k \partial u_k' / \partial x_k \rangle$ is the dissipation tensor, $T_{ij} = \partial \langle u_i' u_j' u_k' \rangle / \partial x_k$ is the turbulent diffusion tensor, $\Pi_{ij} = -\langle u_i' \partial p' / \partial x_j + u_j' \partial p' / \partial x_i \rangle$ is the velocity-pressure-gradient tensor, and $V_{ij} = 1/Re \partial^2 \langle u_i' u_j' \rangle / \partial x_k^2$ is the molecular diffusion tensor.

The negative production observed in the upstream side of the (SW) bump is shown to be due to flow acceleration, $S_{11} > 0$ (figure 3a). Additionally, it is shown that near the wall ($Y < 0.05$) the negative

		$\langle \tau_w \rangle = 0$	θ_{90}	ψ_0	$\gamma_u = 0.5$
SW	x_d	4.41	4.41	4.41	4.40
	x_r	5.38	5.37	5.38	5.38
GW	x_d	4.49	4.45	4.45	4.48
	x_r	5.49	5.55	5.56	5.57

Table 1: Flow separations (x_d) and reattachment (x_r) locations from different criteria computed from the time averaged and z-averaged field for the SW and GW bump.

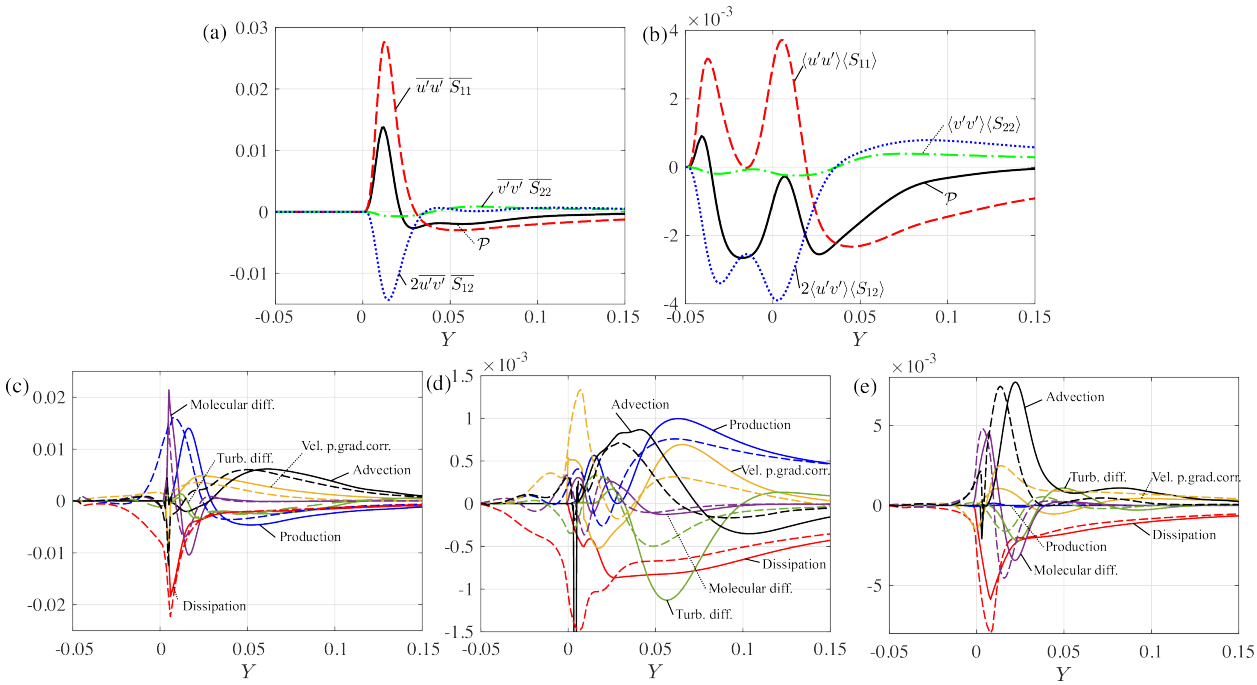

Figure 3: Contributions to TKE production from normal and shear Reynolds stresses in the region of negative production ($x = 4.05$) for (a) SW and (b) GW. Balances for Reynolds stress components (at $x = 4.05$) in the region of negative production: (c) balance of $\langle u'u'\rangle$, (d) balance of $\langle v'v'\rangle$, (e) balance of $\langle w'w'\rangle$; the solid lines correspond to SW and the dashed lines to GW.

production due to Reynolds shear stress is countered by positive contribution of $-\overline{u'u'S_{11}} > 0$. In GW, the negative production at $Y > 0.02$ is similar to that in SW. In contrast, the additional patch of negative production inside grooves is due to negative Reynolds shear stress ($-\langle u'v'\rangle < 0$) and not because of flow acceleration (figure 3b).

In the turbulence statistics section, we discussed that in the region of flow acceleration, the intensity of $\langle u'u'\rangle$ decreases, consistent with the negative production (figure 3c), however $\langle v'v'\rangle$ remains approximately same, and $\langle w'w'\rangle$ even increases. The $\langle v'v'\rangle$ and $\langle w'w'\rangle$ balances reveal that this is predominantly by advection (figures 3d,e). In terms of vortical dynamics, as flow is accelerated, the near wall quasi-streamwise vortices are streamwise stretched and v' and w' intensify, consistent with the increase intensity of $\langle w'w'\rangle$ and maintained intensity of $\langle v'v'\rangle$. Perhaps $\langle v'v'\rangle$ does not increase significantly in magnitude because of a marked loss due to turbulent diffusion, not observed in the balances of $\langle w'w'\rangle$. In GW, the trends at $Y > 0.2$ of the normal Reynolds stresses are similar to SW, while near the wall become too complex to interpret.

The Reynolds stress balances at the peaks of production ($x = 5.1$ for SW and $x = 5.3$ for GW) are shown in figure 4 with the y coordinate normalized by the inflection point, y_{IP}, of the mean streamwise velocity, which collapse the profiles between the SW and GW cases. Note that away from the shear layer, there is no inflection point and hence this scaling is not applicable. Previously Song & Eaton (2004); Schatzman & Thomas (2017) showed that turbulence statistics profiles from a separated flow region collapse with y_{IP} scaling of the y coordinate. Recall, that the GW induces a shift of the peak of turbulence in the wall-normal direction (see section **??**); hence, the scaling of y with y_{IP} is particularly useful to assess the influence of grooves on the profiles. In a simple (equilibrium) shear flow, the production is that of the streamwise normal stress $\langle u'u'\rangle$ (i.e. $\mathcal{P} = 1/2\mathcal{P}_{ii} = 1/2\mathcal{P}_{11}$) and the production of wall-normal, $\langle v'v'\rangle$ and spanwise, $\langle w'w'\rangle$, stresses are by redistribution of energy from the streamwise direction through pressure fluctuations – since $\mathcal{P}_{22} = \mathcal{P}_{33} = 0$ (Pope, 2000). However, in a TBL with a bump perturbation, the mean velocity in the wall-normal direction is non-zero, hence, $\mathcal{P}_{22} \neq 0$ for both SW and GW (figure 4b). In GW, there is non-zero $\mathcal{P}_{33}$, however, at the peak of production we find $\mathcal{P}_{33} \approx 0$, i.e. emphasizing that secondary motions are negligible at this position. Of course, transport terms, as mentioned in the turbulent statistics section,

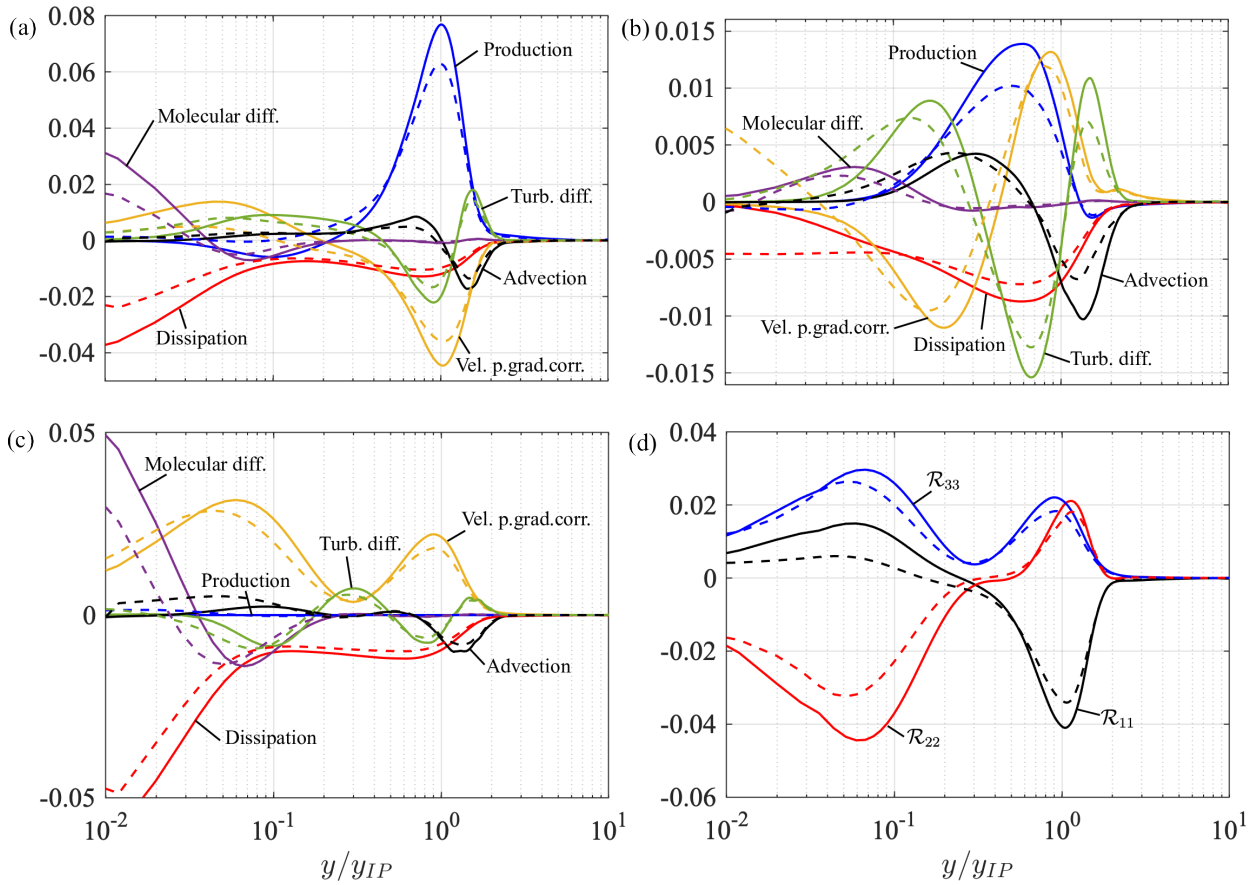

Figure 4: Balances of Reynolds stresses components showing the effect of grooves at the peak location of TKE production: (a) balance of $\langle u'u' \rangle$, (b) balance of $\langle v'v' \rangle$, (c) balance of $\langle w'w' \rangle$, (d) pressure-rate-of-strain redistributive terms ($\mathcal{R}_{11} = \langle p's_{11} \rangle$;$\mathcal{R}_{22} = \langle p's_{22} \rangle$;$\mathcal{R}_{33} = \langle p's_{33} \rangle$). The wall-normal coordinate is normalized by the height of the inflection-point (y_{IP}) in the mean velocity profile. The dashed lines are for GW.

become important, particularly, transport due to pressure fluctuations and turbulent diffusion – the latter more noticeable for $\langle v'v' \rangle$ (figures 4a,b).

The balance of Reynolds stresses gives insight on the production of $\langle w'w' \rangle$, since the peak value of $\langle w'w' \rangle$ is not reduced as much as in the other directions due to the GW. The intensity of $\langle w'w' \rangle$ is predominantly due to the redistribution of energy through pressure fluctuations as seen in figure 4(c). Note that Π_{33} has two peaks, one at the streamwise velocity inflection point and another closer to the wall which in part explains the wider distribution of $\langle w'w' \rangle$ in the wall-normal direction compared to $\langle u'u' \rangle$ and vv.

We further look at the redistribution of energy due to fluctuating pressure revealed by the pressure-rate-of-strain tensor:

$$\mathcal{R}_{ij} = 2\langle p' s'_{ij} \rangle \tag{2}$$

where the rate of transfer of energy among normal stresses exactly balance each other since the trace of $\mathcal{R}_{ij}$ is zero for incompressible flow (i.e. $\mathcal{R}_{11} + \mathcal{R}_{22} + \mathcal{R}_{33} = 0$). At the inflection point, the redistribution of energy is from $\langle u'u' \rangle$ (i.e. loss) to $\langle v'v' \rangle$ and $\langle w'w' \rangle$, but near the wall the loss is predominantly of $\langle v'v' \rangle$ and gain in $\langle w'w' \rangle$ and $\langle u'u' \rangle$ (figure 4d).

S3 Anisotropy evolution

The spatial states of b_{ij} (the normalized anisotropy tensor) can be plotted in the II-III plane, which is known as the Lumley triangle (Choi & Lumley, 2001) or anisotropy invariant map (AIM). For a better graphical representation of the region near the isotropic corner, the invariants are sometimes expressed in a transformed coordinate system(η, ξ), where $\eta^2 = II/3$ and $\xi^2 = III/2$ (Pope, 2000).

The AIM at flow separation ($x = 4.4$) is predominantly a two-component turbulence state in the range of $y = 0$-0.0167 for SW (figure 5a) – as the anisotropy is located at the top line of the triangle. Moving away from the wall (at $x = 4.4$), the flow's invariants transition from two-component axisymmetric turbulence (i.e. $\langle u'u' \rangle$ and $\langle w'w' \rangle$ dominate over $\langle v'v' \rangle$, disk-like) towards the top right corner and one-component turbulence (where $\langle u'u' \rangle$ dominates). For GW, the two-component turbulence, characteristic of a mixing layer, is completely suppressed, and the invariants start in the one-component turbulence at the top corner of the triangle (figure 5a). The invariants in the range $y = 0.0167$-0.15 lie in the right side of the triangle for SW, meaning turbulence anisotropy is rod-like axisymmetric with $\langle u'u' \rangle$ being dominant. The effect of the grooves is to shift the invariant III towards the left side of the triangle, meaning turbulence anisotropy becomes disk-like axisymmetric, which results from a reduction in $\langle u'u' \rangle$. Far from the wall, the invariants approach the origin of the triangle ($\xi = \eta = 0$); thus, the turbulence goes towards a more isotropic state, and the grooves do not affect this.

At $x = 4.55$ (figure 5b), the invariants for the smooth wall are very similar to that at $x = 4.4$. On the other hand, the grooves have a much stronger effect near the wall ($y = 0$-0.0167), and the invariants start closer to the bottom corner, then go towards the two-component turbulence on the left side of the triangle (while still below that for the smooth wall). In addition, the invariants away from the wall ($y = 0.0167$-0.15) go to a one-component state but closer to the bottom corner. At $y \approx 0.15$, the III invariant shift to the left, which further confirms that the grooves reduce the anisotropy of flow near the wall and in the shear layer to have more disk-like turbulence. Farther from the wall ($y = 0.15$-1), only small differences between the grooved and smooth wall are observed.

The invariants at $x = 4.85$ (figure 5c) are completely different between the smooth and grooved wall cases – contrasting to what was observed for the earlier two locations where the trajectories have overall similar shape. First, for the smooth wall case, the invariant starts at the top left corner ($y = 0$), two-component axisymmetric (disk-like). Moving away from the wall, the invariant goes towards the right side of the triangle, two-component axisymmetric (rod-like), and fluctuates along this side. The invariants go from a position closer to isotropic turbulence to one-component turbulence and back again, undergoing axisymmetric contraction and expansion. The grooves effectively suppress the two-component state of turbulence (disk-like) near the wall, and the invariants only fluctuate along the right side of the triangle, as seen for the smooth wall for $y > 0.0167$ for the various wall-normal positions. Nevertheless, in comparison to the smooth wall, the invariants lie closer to the bottom corner in the range $y = 0$-0.15. At $x = 6.5$ (figure 5d), the invariants for the smooth wall case are situated near the left side top corner (disk-like) near the wall ($y = 0$). Moving away from the wall, the invariants transition towards the origin, undergoing axisymmetric expansion, and far

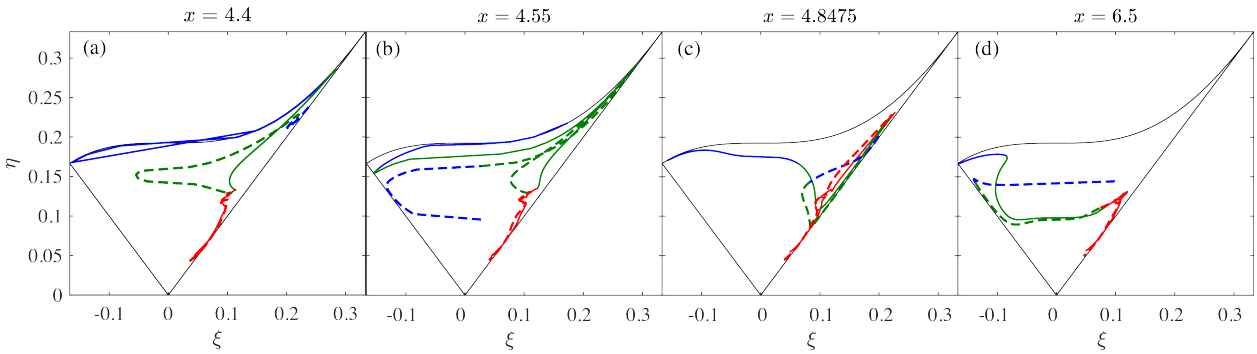

Figure 5: Anisotropy invariant maps at different streamwise positions. The solid and dashed lines represent the smooth and grooved wall, respectively. The colored lines denote different y ranges: blue ($0 < Y < 0.0167$), green ($0.0167 < Y < 0.15$), and red ($0.15 < Y < 1$).

from the wall tends to the right side of the triangle; a pattern also observed in flow past bump perturbations (Mollicone *et al.*, 2017). For the grooved wall case, we observe a continued decrease in anisotropy up to $y = 0.15$.

Although the grooves most strongly modify the flow only near the bump's peak (and the onset of the local shear layer), they notably reduce the anisotropy of the Reynolds stress tensor in the developing local shear layer and past the SB. Thus, history of grooves at the bump peak influences the flow evolution far downstream even when the flow transitions to a flat wall TBL.

References

Bailon-Cuba, Jorge, Leonardi, Stefano & Castillo, Luciano 2009 Turbulent channel flow with 2D wedges of random height on one wall. *International Journal of Heat and Fluid Flow* **30** (5), 1007–1015.

Choi, Kwing So & Lumley, John L. 2001 The return to isotropy of homogeneous turbulence. *Journal of Fluid Mechanics* **436**, 59–84.

Gatti, Davide & Quadrio, Maurizio 2016 Reynolds-number dependence of turbulent skin-friction drag reduction induced by spanwise forcing. *Journal of Fluid Mechanics* **802**, 553–582.

Mollicone, J.-P., Battista, F, Gualtieri, P & Casciola, C M 2017 Effect of geometry and Reynolds number on the turbulent separated flow behind a bulge in a channel. *Journal of Fluid Mechanics* **823**, 100–133.

Na, Y. & Moin, P. 1998 Direct numerical simulation of a separated turbulent boundary layer. *Journal of Fluid Mechanics* **374**, 379–405.

Pope, S. B. 2000 *Turbulent Flows*. Cambridge University Press.

Schatzman, D. M. & Thomas, F. O. 2017 An experimental investigation of an unsteady adverse pressure gradient turbulent boundary layer: Embedded shear layer scaling. *Journal of Fluid Mechanics* **815**, 592–640.

Simpson, R.L., Chew, Y.T. & Shivaprasad, B.G. 1981 The structure of a separating turbulent boundary layer. Part 1. Mean flow and Reynolds stresses. *Journal of Fluid Mechanics* **113**, 23–51.

Simpson, R L 1989 Turbulent Boundary-Layer Separation. *Annual Review of Fluid Mechanics* **21** (1), 205–232.

Song, S. & Eaton, J. 2002 The effects of wall roughness on the separated flow over a smoothly contoured ramp. *Experiments in Fluids* **33** (1), 38–46.

Song, S. & Eaton, J. K. 2004 Reynolds number effects on a turbulent boundary layer with separation, reattachment, and recovery. *Experiments in Fluids* **36** (2), 246–258.

Wu, Wen & Piomelli, Ugo 2018 Effects of surface roughness on a separating turbulent boundary layer. *Journal of Fluid Mechanics* **841**, 552–580.